*Article*

# Initial Radiometric Characteristics of KOMPSAT-3A Multispectral Imagery Using the 6S Radiative Transfer Model, Well-Known Radiometric Tarps, and MFRSR Measurements

**Jong-Min Yeom [1,*], Jisoo Hwang [2], Jae-Heon Jung [1], Kwon-Ho Lee [3] and Chang-Suk Lee [4]**

[1] Cal/Val & Data Quality Control Team, National Satellite Operation & Application Center, Korea Aerospace Research Institute, Daejeon 34133, Korea; jjh583@kari.re.kr

[2] Center for Photometry and Radiometry, Division of Physical Metrology, Korea Research Institute of Standards and Science, Daejeon 34113, Korea; jhwang@kriss.re.kr

[3] Department of Atmospheric & Environmental Sciences, Gangneung-Wonju National University, Gangneung 25457, Korea; kwonho.lee@gmail.com

[4] National Meteorological Satellite Center of Korea Meteorological Administration, Satellite Analysis Division, Jincheon-gun, Chungcheongbuk-do 27803, Korea; lee.changsuk00@gmail.com

* Correspondence: yeomjm@kari.re.kr; Tel.: +82-42-870-3955

**Abstract:** On-orbit radiometric characterization of the multispectral (MS) imagery of the Korea Aerospace Research Institute (KARI)'s Korea Multi-Purpose Satellite-3A (KOMPSAT-3A), which was launched on 25 March 2015, was conducted to provide quantitative radiometric information about KOMPSAT-3A. During the in-orbit test (IOT), vicarious radiometric calibration of KOMPSAT-3A was performed using the Second Simulation of a Satellite Signal in the Solar Spectrum (6S) radiative transfer model. The characteristics of radiometric tarps, the atmospheric optical depth from multi-filter rotating shadowband radiometer (MFRSR) measurements, and sun–sensor–geometry were carefully considered, in order to calculate the exact top of atmosphere (TOA) radiance received by KOMPSAT-3A MS bands. In addition, the bidirectional reflectance distribution function (BRDF) behaviors of the radiometric tarps were measured in the laboratory with a two-dimensional hyperspectral gonioradiometer, to compensate for the geometry discrepancy between the satellite and the ASD FieldSpec® 3 spectroradiometer. The match-up datasets between the TOA radiance and the digital number (DN) from KOMPSAT-3A were used to determine DN-to-radiance conversion factors, based on linear least squares fitting for two field campaigns. The final results showed that the $R^2$ values between the observed and simulated radiances for the blue, green, red, and near-infrared (NIR) bands, are greater than 0.998. An approximate error budget analysis for the vicarious calibration of KOMPSAT-3A showed an error of less than 6.8%. When applying the laboratory-based BRDF correction to the case of higher viewing zenith angle geometry, the gain ratio was improved, particularly for the blue (1.3%) and green (1.2%) bands, which exhibit high sensitivity to the BRDF of radiometric tarps during the backward-scattering phase. The calculated gain ratio between the first and second campaigns showed a less than 5% discrepancy, indicating that the determined radiometric characteristics of KOMPSAT-3A are reliable and useful to the user group for quantitative applications.

**Keywords:** KOMPSAT-3A; vicarious calibration; 6S radiative transfer model; radiometric tarps; laboratory-based BRDF; MFRSR; PSF

## 1. Introduction

The recently developed Korea Multi-Purpose Satellite-3A (KOMPSAT-3A), which is a continuation of the KOMPSAT-1–3 earth observation satellite (EOS) programs from the Korea Aerospace Research Institute (KARI), was launched on 25 March 2015, on a Dnepr-1 launch vehicle from the Jasny Dombarovsky site in Russia. The main purpose of the KOMPSAT-3A is to enable us to take advantage of geographical information systems (GIS) in environmental, agricultural, and oceanographic sciences, and to facilitate natural hazards. After the launch, KARI performed an in-orbit test (IOT) that included radiometric calibration for a six month period between 14 April and 4 September 2015. KOMPSAT-3A is equipped with two distinctive sensors, a high-resolution multispectral (MS) optical sensor, namely the Advanced Earth Image Sensor System-A (AEISS-A), and the Scanner Infrared Imaging System (SIIS). In this study, we focused on the radiometric calibration of AEISS-A.

The radiometric calibration of the optical satellite is a prerequisite for quantitative applications of remote sensing [1], in order to make full use of the physical data for Earth observation (EO) and also for radiometric data continuity with different EO satellites [2]. Although most EO satellite sensors are carefully calibrated by a laboratory experiment with a characterized radiance source, defining absolute radiometric calibration is a challenge after the launch, due to inevitable in-orbit modifications by effects such as the outgassing phenomenon (in early stages) and radiation emissions (on a longer-term scale), that affect both the optical transmission and the charge-coupled device (CCD) signal in darkness [3]. Furthermore, the device sensitivity for converting the digital number (DN) into radiance values degrades over time, mainly because of sensor deterioration [4,5]. Various radiometric calibration methods have been suggested to calibrate most of the operating radiometric sensors, such as Landsat 7/8, IKONOS, QuickBird, Pleiades, RSI, and SSOT [6–10]. In-orbit calibration methods include onboard, vicarious, cross, star, and lunar calibration [7,11,12]. Generally, cross-calibration or onboard calibration uses well-calibrated satellites or well-defined radiance sources on satellites, while vicarious calibration is completed using measurable natural or artificial reflectors. In this study, we vicariously calibrated the device using radiometric tarps. The same locations are revisited very infrequently, due to the narrow swath width and high spatial resolution of KOMPSAT-3A. This makes it difficult to acquire stable and predictable reflectances using natural reference targets such as deep convection clouds [13], dark reflectance surfaces [14], and oceans [15]. Furthermore, it is difficult to acquire various reflectance ranges from dark to bright natural targets, in order to effectively determine the DN to radiance empirical line within a regular time period.

The main purpose of this paper is to report on the initial conditions of the radiometric calibration of KOMPSAT-3A during the IOT periods, performed on the basis of vicarious calibration methods. In this study, the Second Simulation of the Satellite Signal in the Solar Spectrum (6S) radiative transfer model [16] was used to simulate the amount of radiance observed by the sensor at the top of atmosphere (TOA) level. The radiometric calibration method of KOMPSAT-3A is based on the previous KOMPSAT-3 vicarious algorithm [17], but the input data processing for the 6S radiative transfer model was improved. We carefully processed the input data, such as laboratory-based bidirectional reflectance distribution function (BRDF) measurements of each of the tarp samples, with a hyperspectral gonioreflectometric instrument for BRDF correction, and multifilter rotating shadowband radiometer (MFRSR) measurements for atmospheric constituent parameterization. These measurements included the aerosol optical depth (AOD), amount of water vapor, and point spread function (PSF) simulations of AEISS-A with star observations, which can be compared with a previous study [17], because accurate input parameters lead to accurate simulations of the TOA radiance, received by each of the KOMPSAT-3A MS bands. Based on carefully prepared input parameters, we estimated the simulated TOA radiance received by KOMPSAT-3A MS and compared it with the KOMPSAT-3A DN in order to determine the DN-to-radiance coefficients, which indicated that radiometric conversion information is useful for the quantitative application user group.

## 2. Materials and Methods

Table 1 represents the detailed specifications of the KOMPSAT-3A AEISS-A sensors. KOMPSAT-3A is a newly developed satellite of KOMPSAT-3 with higher spatial resolution, and is equipped with the SIIS IR sensor, but with the same MS imagery specifications. The spectral response functions and panchromatic bands are the same as those used with the KOMPSAT-3 MS. Under a nominal orbit, its ground sample distance (GSD) for multi-spectral images and panchromatic images is 2.2 m and 0.55 m, respectively. The swath width of KOMPSAT-3A is less than 12 km at nadir direction, and its expected lifetime is designed to be four years.

**Table 1.** Detailed specifications of the KOMPSAT-3A AEISS-A.

| Mission Characteristic | Information |
|---|---|
| Design lifetime | 4 years |
| Orbit altitude | 528 km |
| Swath width | $\geq$12 km (at nadir) |
| Ground sample distance | PAN: 0.55 m (altitude 528 km)<br>MS: 2.2 m (altitude 528 km) |
| Spectral bands | Pan 450–900 nm<br>Blue 450–520 nm<br>Green 520–600 nm<br>Red 630–690 nm<br>NIR 760–900 nm |
| Radiometric Resolution | 14 bit |
| Modulation Transfer Function (MTF) | PAN $\geq$ 10%<br>MS $\geq$ 13% |
| Signal-to-Noise Ratio (SNR) | 100 |

In this study, we selected two field campaign sites, Goheung (GH) County, South Korea (34.60°N, 127.20°E), and Zuunmod, Mongolia (MG) (47.721°N, 107.064°E). The locations of the field campaigns are shown in Figure 1a,b. In the first field campaign at Goheung (Figure 1a), we obtained cropped images of the tarp areas from the KOMPSAT-3A MS, and their corresponding unmanned aerial vehicle (UAV) images. These images are shown in Figure 1c,e, respectively. We used the 10 × 20 m tarps numbered from one to four, shown to the right of Figure 1e. We chose these over the smaller 10 × 10 m tarps to mitigate the PSF effects caused by the CCD camera [18]. These can be reduced by increasing the spatial extent of the target. The 10 × 20 m tarps shown in Figure 1c were represented by 5 × 10 pixel regions in the images. The edges, which were clearly influenced by the surrounding reflectance, are semitransparent. By visually inspecting these tarp areas, we can see that they are represented by areas of 3 × 8 pixels. Only pixels that were clearly part of the tarp area were used to determine the ground reference values for the KOMPSAT-3A DN. According to [19], in order to obtain reasonable vicarious radiometric calibration results, the radiometric tarp must occupy an area of 5 × 5 pixels or more when observed from the satellite. The authors of that study used 20 × 20 m tarps to vicariously calibrate IKONOS satellites. The spatial resolution of the IKONOS satellites was 4 m. As the KOMPSAT-3A satellites have an MS channel spatial resolution of 2.2 m, areas represented by 5 × 5 pixels, which correspond to areas of 11 × 11 m or larger, can be used for vicarious calibration. The tarps used in the Goheung field observations were sufficiently large in the vertical direction, but 1 m too small in the horizontal direction. This made environmental effects more pronounced. In the second field campaign over Zuunmod (Figure 1b,d,f), we used larger radiometric tarps with dimensions of 20 × 20 m, as shown in Figure 1d,f. In Figure 1d, we can see that the areas which are clearly tarps, occupy a minimum of 8 × 8 pixels in the KOMPSAT-3A MS images. Hence, for vicarious calibration, it is better to use larger radiometric tarps, like those used in the second field campaign. The observations of these tarps were less affected by the environment.

When fabricating the radiometric tarps, we selected reflectance rates in the range 3% to 56%. We assumed that these rates would facilitate the radiometric calibration process, as, according to previous studies [20], the natural reflectance of land to light in the visible to NIR spectrum is usually less than 60%.
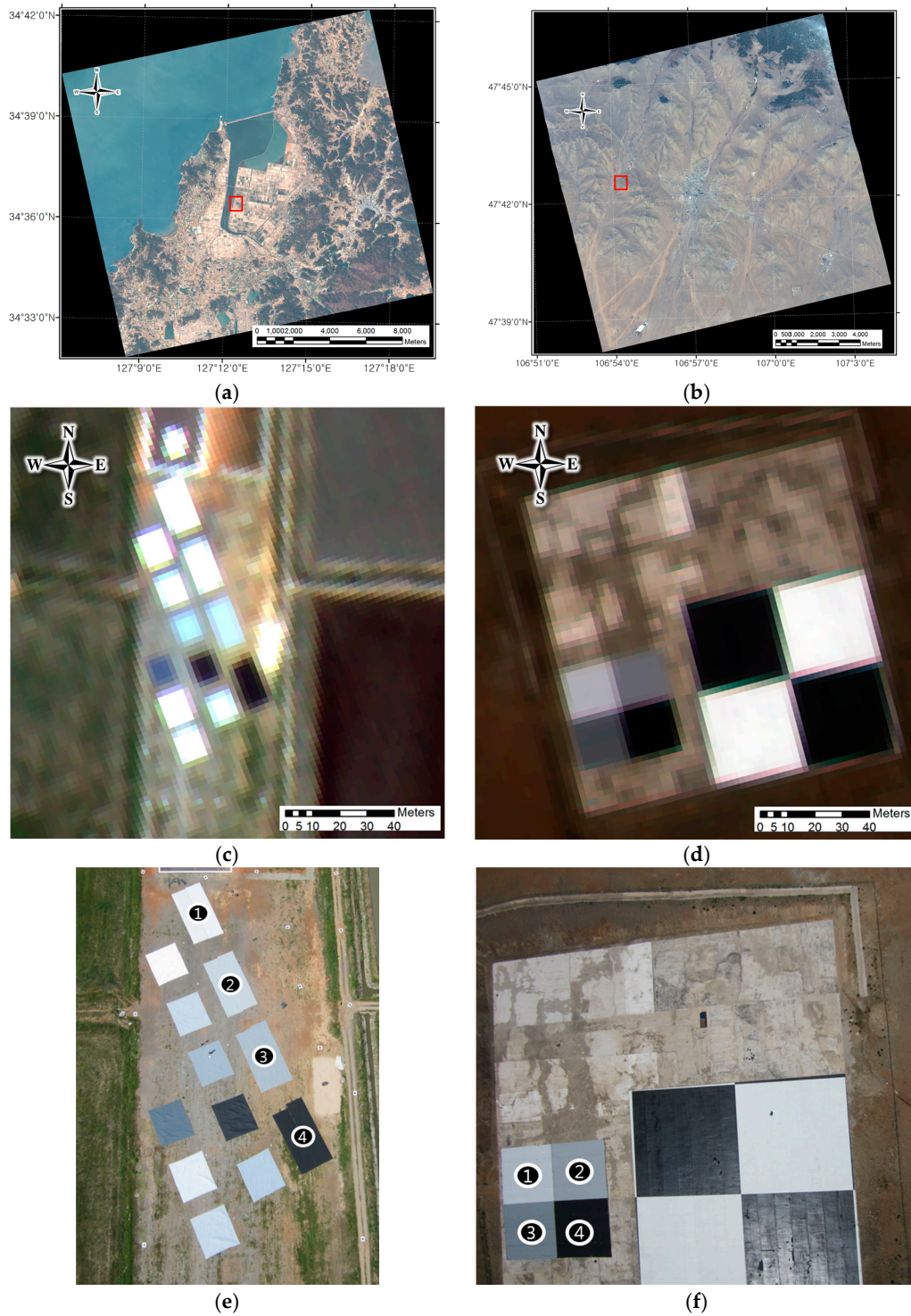


(a)



(b)



(c)



(d)



(e)



(f)

**Figure 1.** *Cont.*

(**g**)

**Figure 1.** (**a**) KOMPSAT-3A RGB image of Goheung County, South Korea, acquired on 27 March 2015 and (**b**) KOMPSAT-3A RGB image of Zuunmod, Mongolia, acquired on 18 June 2015. (**c**,**d**) are cropped KOMPSAT-3A MS images of the tarp areas in Goheung and Zuunmod. These areas correspond to the red squares in (**a**,**b**). Finally (**e**,**f**) are UAV RGB images taken before satellite pass time and show the locations of the deployed radiometric tarps. (**g**) A picture of the MFRSR instruments deployed at the Goheung site.

*2.1. Schema of Vicarious Calibration Algorithm for KOMPSAT-3A Using 6S Radiative Transfer Model*

In this study, we adopted the 6S radiative transfer model to simulate the physical radiance received by the KOMPSAT-3A MS sensor by retrieving the essential model input parameters. The 6S code, which is the improved version of 5S, includes a more accurate calculation of highly asymmetric aerosol scattering phase functions, arbitrary variation in the vertical aerosol profile, the ability to change the number of calculation angles and layers, and an increased number of node wavelengths from 10 to 20. The 6S radiative transfer model was validated by Kotchenova et al. [21] and found to be consistent to within 1%, when compared with other RTMs [22]. The model has been extensively validated, and its accuracy is stated to be within 1% [23]. Therefore, securing accurate input parameters allows an exact atmospheric parameterization calculation, and it is imperative that such input parameters be considered and retained in order to estimate accurate DN-to-radiance coefficients. In this study, we improved the accuracy of the vicarious radiometric calibration algorithm by both improving the existing input data calculation method, and introducing a new method that was not used in the previous radiometric calibration study [17]. Figure 2 presents a flowchart of the vicarious radiometric calibration of KOMPSAT-3A using the 6S radiative transfer model and related input parameters. The main input parameter processes, such as the hyperspectral reflectance of tarps from ASD FieldSpec® 3, laboratory-based BRDF measurements, precise atmospheric measurements from MFRSR, and PSF correction, were carefully applied to accurately calculate the amount of sensor-received radiance.

In addition, ancillary input parameters, such as geometric conditions, the spectral response function (SRF) for KOMPSAT-3A MS bands, and environmental surface reflectance, were also considered. To consider the background surface reflectance, we introduced an environmental function that models adjacency effects. This function takes into account the scattering effects induced by the difference in reflectance between the tarp and the surrounding area. We assumed that the surface reflectance was not uniform, as is the case with a circular target. In the 6S model, the adjacency effects were calculated based on the target reflectance, the target radius, and the environmental reflectance. We used surface spectral libraries from the Korean Institute of Geoscience and Mineral Resources (KIGAM) to determine the environmental reflectance. For more information, see the 6S radiative transfer model manual [24].
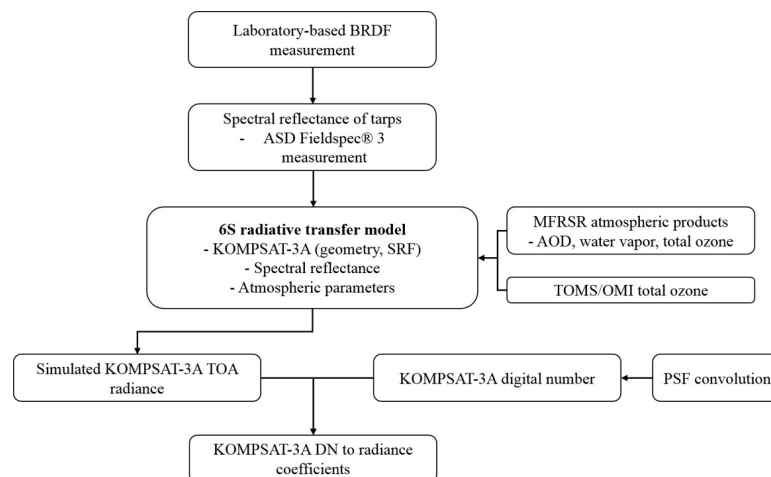
**Figure 2.** Flowchart of vicarious radiometric calibration of KOMPSAT-3A using the 6S radiative transfer model and related input parameters.

Table 2 shows the KOMPSAT-3A geometric conditions for the vicarious radiometric calibration during the two field campaigns. Until we had acquired a useful KOMPSAT-3A calibration dataset, satisfying the clear-sky weather conditions and reliable geometric conditions with a viewing angle of less than 10 degrees, we had to command new observation orders for KOMPSAT-3A more than 10 times. During the IOT period, we finally acquired two calibratable KOMPSAT-3A images, with a viewing zenith angle of less than 10 degrees under clear-sky conditions. The first one was acquired on 27 May 2015 at 04:43 coordinated universal time (UTC), over Goheung, and the second was acquired on 18 June 2015 at 05:47 UTC, over Zuunmod (Table 2).

**Table 2.** Geometric conditions of KOMPSAT-3A for vicarious calibration.

| Site | Date | Overpass Time (UTC) | Solar Zenith | Solar Azimuth | Viewing Zenith | Viewing Azimuth |
|---|---|---|---|---|---|---|
| Goheung, South Korea | 27 May 2015 | 04:43:42 | 21.29 | 236.04 | 9.92 | 261.39 |
| Zuunmod, Mongolia | 18 June 2015 | 05:47:01 | 26.58 | 208.74 | 2.76 | 78.60 |

Based on the size of the tarps at each location, we expected to observe reduced adjacency effects in the Zuunmod tarps, due to their ability to secure more purely reflected spectral reflectances compared to the first field campaign. Furthermore, the viewing zenith angle of KOMPSAT-3A during the Zuunmod field campaign was less than that of the first field campaign (see Table 2), indicating that reduced effects of BRDF surface tarps and atmospheric loads could be expected.

*2.2. ASD FieldSpec® 3 Measurements of the Hyperspectral Reflectance of Tarps*

As mentioned previously, we deployed radiometric tarps before the expected KOMPSAT-3A pass time, as shown in Figure 1e,f. To estimate the high-spectra resolution of the reference targets, we utilized an ASD FieldSpec® 3 (ASD Inc., Boulder, CO, USA). This is a high-resolution spectroradiometer with a spectral resolution of 3 nm in the 350–1000 nm spectral range, and 10 nm in the 1000–2500 nm spectral range. The full spectral range of the spectroradiometer covers the KOMPSAT-3A MS bands (450–950 nm). Thus, the spectra of the radiometric tarps can be used as surface reference data. When performing ASD FieldSpec® 3 measurements, it is important to use appropriate observation geometries and measurement times. To normalize the reflectance and reduce the BRDFs caused by the differences in the ASD FieldSpec® 3 geometry and the changeable KOMPSAT-3A geometry [25], we fixed the ASD observation geometry in the direction of the nadir. Then, we carefully measured the spectra of the radiometric tarps using the ASD FieldSpec® 3. To reduce temporal observation

discrepancies and the effects of changes in the solar zenith angle on the BRDF, we took these measurements in the hour before the KOMPSAT-3A passed over the tarps. When measuring the hyperspectral reflectance of the tarps using the ASD FieldSpec® 3, we ensured that the results reflected the spatial radiometric characteristics of the targets, by measuring points on each tarp at least 20 times, with 10 repetitions per measurement. The mean value of these measurements was used in simulations of the 6S model. The reflectance differed by less than 1% between any two points in each tarp. As shown in Figure 3, all of the spectral reflectance curves of the four large tarps produced a spectrally flat pattern, with the exception of the starting points. As shown on the spectral curve, the reflectance of the radiometric tarps used in the second field campaign was constant over the spectral wavelength band. This indicates that the reflectances of the tarps measured at a resolution of 1 nm, could be used as reference surface values in simulations of the 6S radiative transfer model.
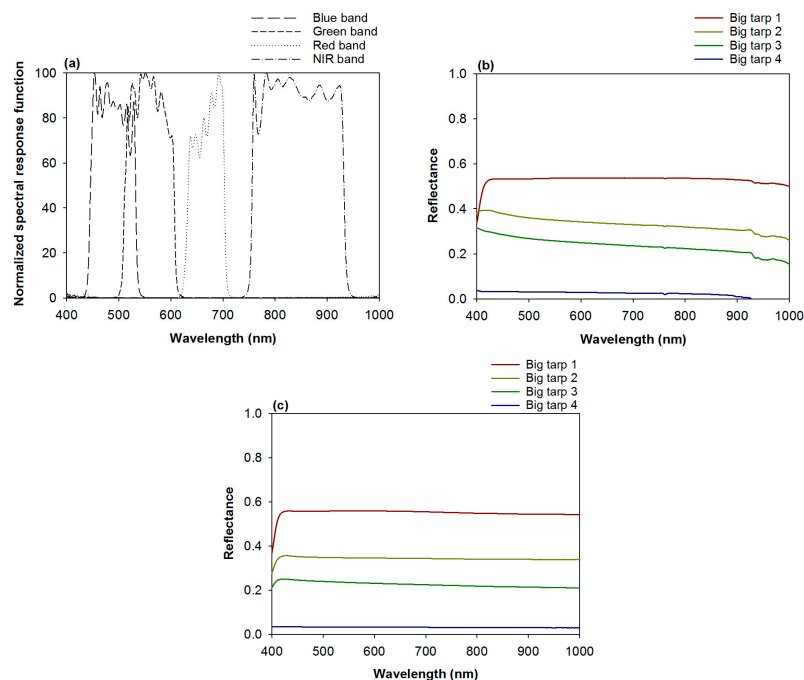
**Figure 3.** (**a**) Relative SRF curves for KOMPSAT-3A and measured surface tarp reflectances from the ASD FieldSpec® 3 for the first Goheung (**b**) and second Zuunmod (**c**) Field campaigns.

### 2.3. Laboratory-Based BRDF Measurements of Radiometric Tarps

The BRDF measurement is generally used to infer reflectance at a given viewing geometry and to compute a hemispheric albedo from a reflectance measurement made from a specific direction [26]. The accuracy of such tarp-based field calibrations depends on an accurate knowledge of the tarps' laboratory-measured BRDF at a variety of source illuminations and detector scatter angles [27], as the BRDF effect is considered an unknown amount of error in the reflectance values [28]. We performed laboratory-based BRDF measurements of the radiometric tarps to compensate for the observation discrepancy between nadir-direction ASD FieldSpec® 3 measurements, and solar target sensor-dependent KOMPSAT-3A geometry. First, we cut edge sections (30 cm × 30 cm) from each of the deployed radiometric tarps to measure BRDF in the laboratory. The radiometric tarp samples were made from chemically-treated canvas. We measured the BRDF characteristics of the deployed tarps according to the angle of incidence and reflection, using a hyperspectral gonioreflectometer designed to measure two-dimensional BRDFs for the principal plane. The hyperspectral gonioreflectometer consists of a source system and a goniometric detection system, as shown in Figure 4 [29]. The source system has dual sources: a Xe lamp emitting wavelengths in the 380–780 nm range, and a super-continuum laser emitting wavelengths in the 450–1000 nm range. As its wavelength range covered the spectral

bands of the KOMPSAT-3A AEISS-A sensors, the super-continuum laser source was used for the BRDF measurements. The beam was adjusted with two lenses and an aperture, and then directed toward the sample. The goniometric detection system had a central axis with two-rotational stages, one for the sample and one for the detection system. We used a three-axis translational stage to adjust the position of the sample and the sample plane to the central axis. The detection system had an aperture that was used to define the solid angle of detection in the reflected radiance measurements, and a fiber-optic probe connected to a CCD-based spectroradiometer with a bandwidth of 3 nm. The instrument used an absolute method to measure the BRDF: the incident irradiance was measured with the sample translated away from the beam path, and the detection system positioned along the beam path. To measure the reflected radiance, the sample was positioned in the beam path, and the detection system was positioned at the angle of reflection.



(**a**)                    (**b**)
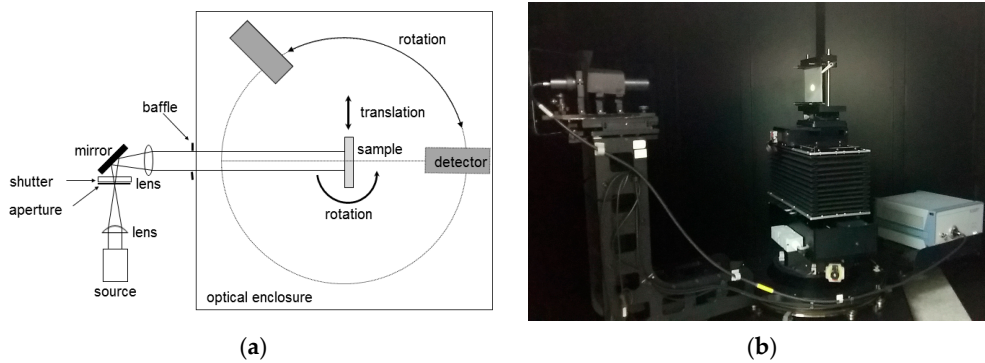
**Figure 4.** Schematic (**a**) and photograph (**b**) of the hyperspectral gonioreflectometer used for BRDF measurements on tarps.

Based on the laboratory BRDF measurements, anisotropy factors (ANIFs) of each radiometric tarp were estimated using the following equation [28]:

$$ANIF(\theta_i; \theta_r; \lambda) = \frac{BRDF(\theta_i; \theta_r; \lambda)}{BRDF_N(\theta_i; \theta_n; \lambda)} \tag{1}$$

where $BRDF(\theta_i; \theta_r; \lambda)$ is the BRDF for illumination radiance that comes from elevation ($\theta_i$) directions, which is reflected to elevation directions ($\theta_r$) at wavelength $\lambda$ in the principal plane. Basically, $BRDF(\theta_i; \theta_r; \lambda)$ was intended for the BRDF measurement of KOMPSAT-3A geometry for the Goheung and Zuunmod field campaigns. $BRDF_N(\phi_i, \theta_i; \phi_r, \theta_N; \lambda)$, which corresponds to the nadir-direction-measured ASD FieldSpec® 3 result, is measured in the nadir direction ($\theta_n = 0°$). The ANIF is an intuitive reflectance anisotropy measure that varies in theory between 0 and $\infty$ [30].

The values for each of the field campaign geometries are estimated to normalize the MS reflectance of KOMPSAT-3A to the nadir direction, corresponding to the ASD FieldSpec® 3 observation based on following equation:

$$\rho'(\theta_i; \theta_i; \lambda) = \frac{\rho(\theta_i; \theta_i; \lambda)}{ANIF(\theta_i; \theta_i; \lambda)} \tag{2}$$

where $\rho'$ is the normalized MS reflectance of KOMPSAT-3A in the nadir direction, and $\rho$ is the original reflectance of KOMPSAT-3A for the instantaneous geometry conditions in Table 2. In previous studies [17], laboratory-based BRDF measurements have been made and directional uncertainties for radiometric tarps were calculated, but no corrections were made for actual KOMPSAT-3 images. In the previous study, the solar zenith angle and the viewing zenith angle were measured at 10 degree intervals. Due to errors in the process used to interpolate between the intervals, only the uncertainty due to measurements of the tarp was shown. In this study, we used actual KOMPSAT-3A geometric conditions, shown in Table 2, to correct for the fact that we were using satellite images.

Figures 5 and 6 show the estimated ANIF values according to each radiometric tarp (from 4% to 60% reflectance), obtained by reflecting the geometries of the Goheung and Zuunmod field campaigns, respectively. For example, in Figure 5, for estimating ANIF, the laboratory-based BRDF measurement geometry condition is 21.3° incidence with ±9.9° detection (negative is backward scattering and positive is forward scattering), which is the same as the satellite observation geometry for the Goheung field campaign. In Figure 6, the experiment geometry condition is 26.6° incidence with ±2.9° detection, the same as the Zuunmod field campaign. As shown in Figure 5, we found slightly inverse symmetrical patterns of ANIF values for all radiometric tarps, except for the 4% tarp, indicating two important facts. The first is that the changeable sun–tarp–sensor geometry should be considered, in order to determine which scattering phases would be reflected by checking geometrical conditions. The second is that radiometric tarps would be expected to have effects on BRDF values in the azimuth direction. We inferred that the inverse symmetry of BRDF values between backward and forward scattering originated from the dependence of the tarps' weft and warp thread orientations on the diffuse reflectance [27]. Under backward scattering conditions, the ANIF values, and even the uncertainties, deviated from 1, except for the 60% tarp, which approached 1 as the wavelength increased (Figure 5a,c,e,g). This means that the effects of the radiometric tarps on BRDF are more effective for shortwave ranges, such as the blue and green bands. In the case of forward scattering, not only were ANIF values near 1, but an ANIF value of 1 was included in the uncertainty range over most of the measurement wavelengths (Figure 5b,d,f,h). For the Goheung field campaign site (Table 2), the ANIF value for backward scattering was applied, in order to normalize the satellite reflectance, because the relative azimuth angle between satellites and the sun is 25.4°.

In the case of the Zuunmod field campaign, because the site has a decreased viewing zenith angle (detection angle) compared to the Goheung site, weaker BRDF effects, which are sensitive to the extent of off-nadir direction, would be expected. Therefore, inevitably, the ANIF values and the uncertainties were near 1, indicating that the radiometric tarps of the Zuunmod field campaign with a +2.9° viewing zenith angle, have weak effects on the BRDF.

We only applied ANIF-based correction for the Goheung site, based on the laboratory BRDF measurements using Equation (2).
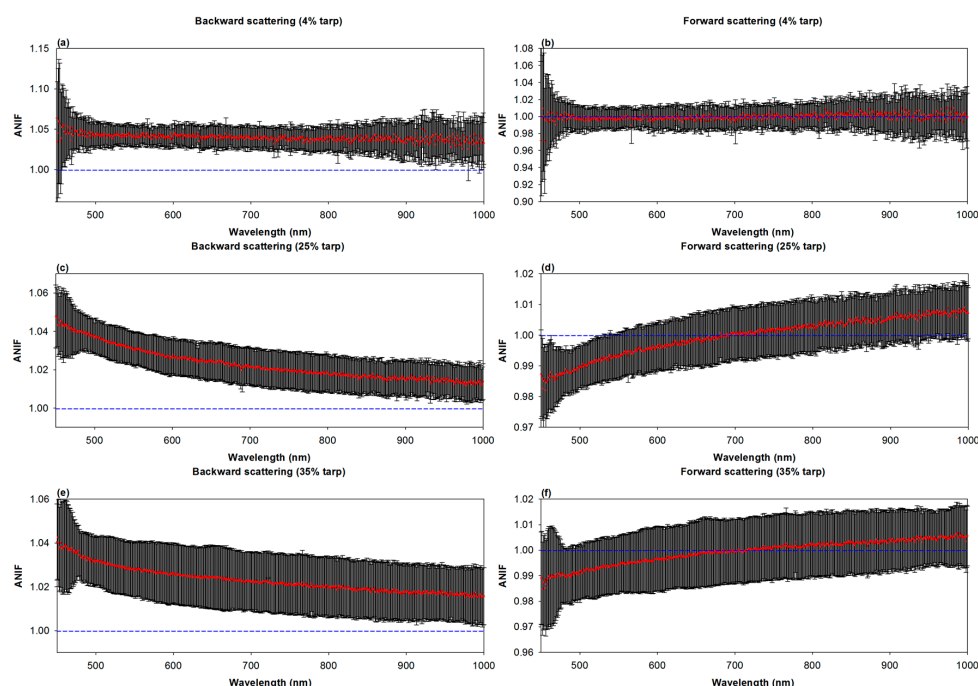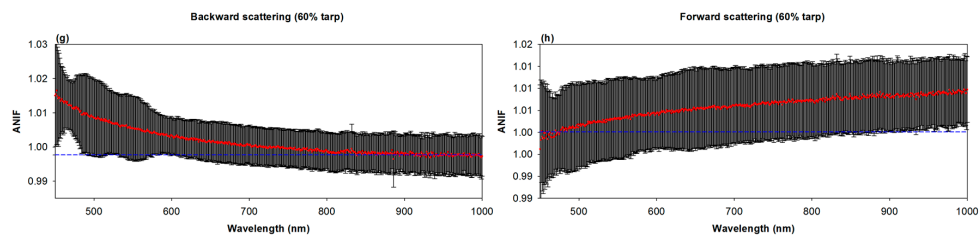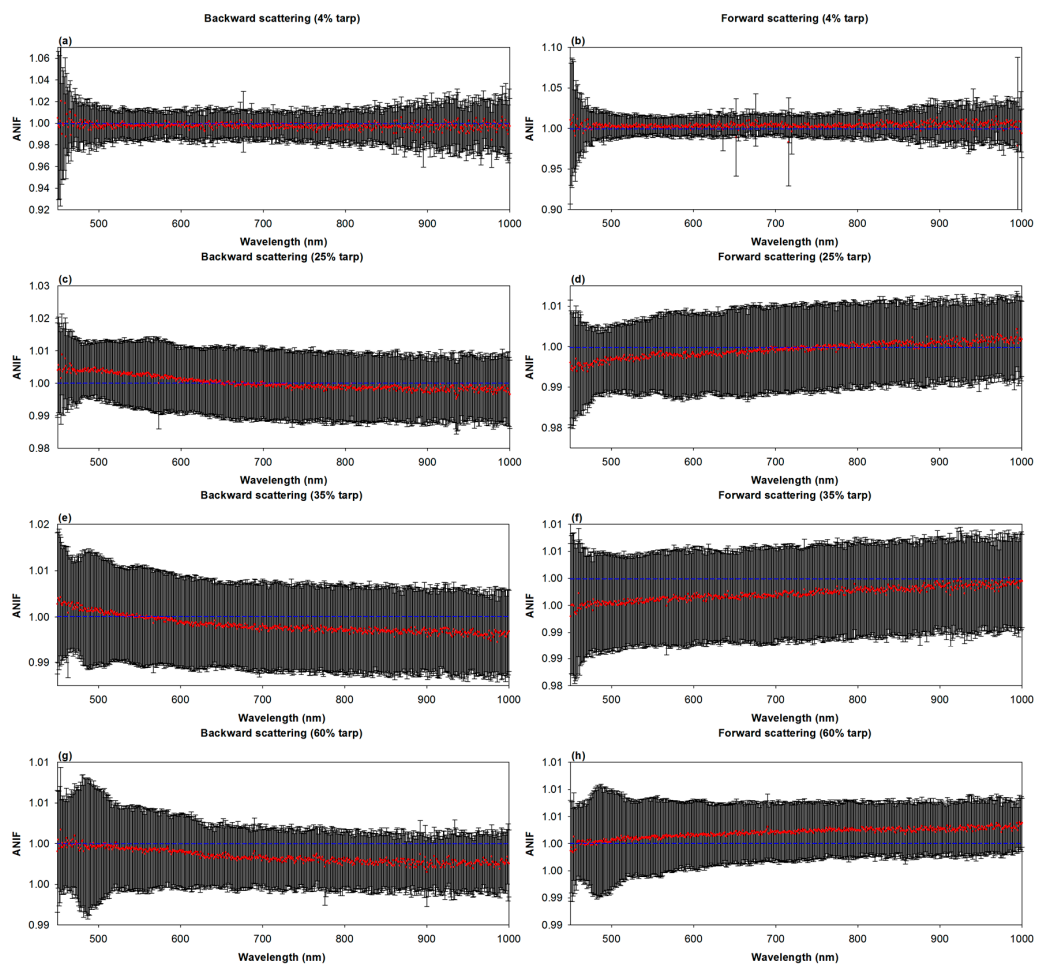


**Figure 5.** *Cont.*

**Figure 5.** Measured ANIF values (red points) for the Goheung field campaign sites. The vertical error bar is the uncertainty, and the blue dashed line represents an ANIF of 1, meaning that no BRDF effect is expected. (left panel, **a**,**c**,**e**,**g**) are the ANIF of 4%, 25%, 35% and 60% tarp under backward scattering condition, and (right panel, **b**,**d**,**f**,**h**) are the ANIF of 4%, 25%, 35% and 60% tarp under forward scattering condition.



**Figure 6.** Measured ANIF values (red points) for the Zuunmod field campaign sites. The vertical error bar is the uncertainty, and the blue dashed line represents an ANIF of 1, meaning the value where no BRDF effect would be expected. (left panel, **a**,**c**,**e**,**g**) are the ANIF of 4%, 25%, 35% and 60% tarp under backward scattering condition, and (right panel, **b**,**d**,**f**,**h**) are the ANIF of 4%, 25%, 35% and 60% tarp under forward scattering condition.

### 2.4. Atmospheric Conditions Using MFRSR for AOD and Column Water Vapor

In this study, we used MFRSR observation equipment to obtain accurate atmospheric data. In our previous study, we used less accurate MODIS equipment, so the uncertainty in our measurements was higher [17]. The MFRSR has been used to measure atmospheric parameters, such as AOD and water

vapor [31,32]. For the atmospheric parameterization, MFRSR-measured AOD and column water vapor were used as input parameters to derive sensor-level radiance.

In the case of AOD estimation with MFRSR, we first measured the total, direct, and diffuse irradiances at the Goheung and Zuunmod field campaign sites. In general, the well-known Langley regression method is widely used to estimate AOD by retrieving the TOA irradiance ($I_0$), by securing at least two months of continuous measurements that are long enough to reduce the statistical variability to less than 1% per day [33]. However, it is difficult to acquire long-term continuous observations during vicarious calibration field campaign periods. In this study, to overcome this limitation of the Langley regression method, the modified Langley correction method, using the maximum value composite (MVC) of the largest irradiance values at a given air mass, was applied. Lee et al. [34] proved that the suggested MVC-based Langley method (hereafter, Langley$_{MVC}$) showed reasonable statistical results for nearly impossible-to-find days that meet the requirements for performing traditional Langley analyses.

Figure 7 shows an example of the Langley plots of the MFRSR 496 nm channel irradiance data as functions of air mass, for Goheung and Zuunmod. The Langley$_{MVC}$ cannot deal with temporal changes in $I_0$ during a given composite period; therefore, the smoothing and removal of outliers using a filtering technique were employed from one composite period to another [35]. The correlation coefficients for Goheung and Zuunmod were 0.996 and 0.982, respectively, indicating that the $I_0$ from Langley$_{MVC}$ would be useful for deriving the total optical depth (TOD) during the field campaigns.
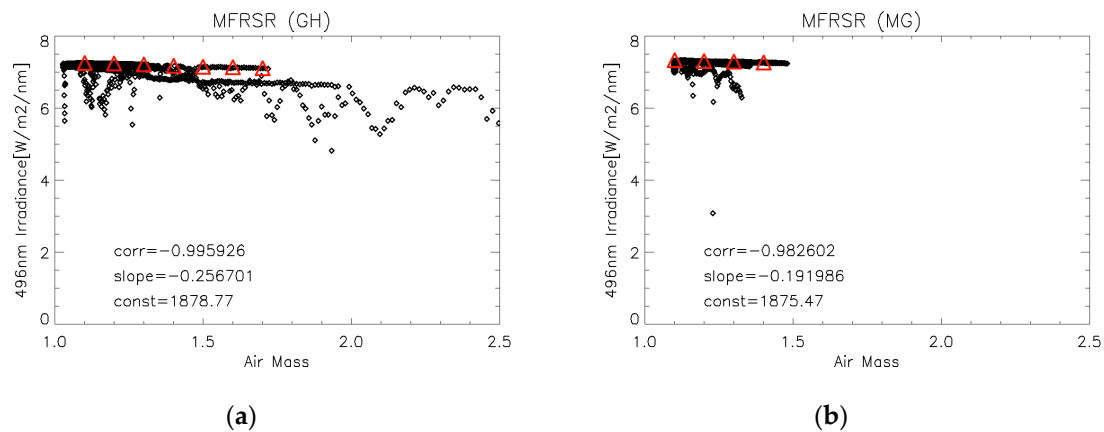


**Figure 7.** Langley plots for MFRSR 496 nm channel data for (**a**) the Goheung (GH) site acquired on 27 May 2015, and (**b**) the Zuunmod site in Mongolia (MG) acquired on 18 June 2015. The red triangles are selected bins from the maximum values result of the Langley curves.

Based on the $I_0$ determined from Langley$_{MVC}$, TOD ($\tau_{Tot}$) was estimated using the following equation:

$$\tau_{Tot} = \frac{1}{m} \ln\left(\frac{I}{I_0}\right) \tag{3}$$

where $I$ is the instantaneous direct solar irradiance from the MVC method and m is the air mass. The TOD during any time of the day consisted of the Rayleigh optical depth (ROD, $\tau_{Rayleigh}$), AOD ($\tau_{aerosol}$), and gas absorption optical depth (GAOD, $\tau_{gas}$), as follows:

$$\tau_{Tot} = \tau_{Rayleigh} + \tau_{aerosol} + \tau_{gas} \tag{4}$$

Therefore, AOD can be derived by subtracting ROD and GAOD, from TOD. ROD can be calculated as a function of wavelength ($\lambda$) [36], as follows:

$$\tau_{Rayleigh} = 0.008569\lambda^{-4} \times \left(1 + 0.0113\lambda^{-2} + 0.00013\lambda^{-4}\right) \tag{5}$$

Although gas absorption is effectively zero for many regions of the solar spectrum, ozone absorption at the 496, 615, and 670 nm wavelengths, and $NO_2$ absorption at the 415, 496, and 615 nm MFRSR wavelength channels, are sensitive [33,37], and must be taken into account. Therefore, the optical depths of ozone absorption and $NO_2$ absorption were estimated using the corresponding ozone absorption coefficients [38] and $NO_2$ absorption cross-sections [39], following Equations (6) and (7), respectively:

$$\tau_{O3} = \sigma_{O3} \times D_{O3}/1000 \tag{6}$$

$$\tau_{NO2} = \sigma_{NO2} \times D_{NO2}/1000 \tag{7}$$

where $\sigma_{O3}$ in $cm^{-1}$ is the ozone absorption coefficient and $D_{O3}$ is the total column ozone in Dobson units (DU) from the Total Ozone Mapping Spectrometer (TOMS) instrument and the Ozone Monitoring Instrument (OMI). Similarly, total column $NO_2$ ($D_{NO2}$) from the OMI was used to derive $NO_2$ absorption ($\sigma_{NO2}$). In this study, we used the TOMS OMI total ozone as the input parameter for the 6S model to simulate ozone absorption.

Figure 8 shows the final results of MFRSR AOD over Goheung and Zuunmod. The scattered patterns of Goheung in the morning were caused by passing clouds, according to visual inspection of Geostationary Ocean Color Imager (GOCI) RGB images. Afterwards, all spectral channels showed stable AOD curves. The Zuunmod field campaign site showed more stable AOD curves and longer periods of clear skies. For both sites, the estimated AODs could be used as an input parameter of the 6S radiative transfer model.
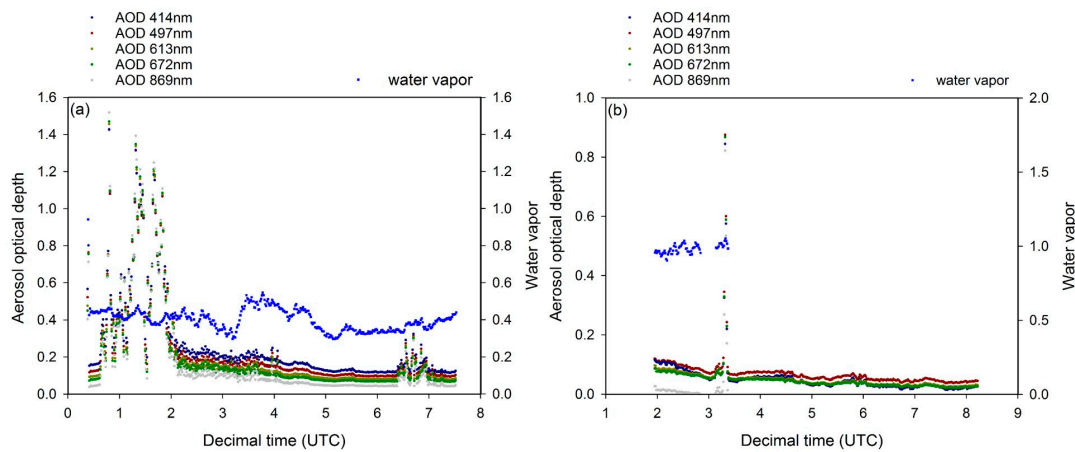


**Figure 8.** Temporal AOD and column water vapor (blue dots) using MFRSR measurements for the Goheung (**a**) and Zuunmod (**b**) field campaigns.

Among the seven MFRSR channels, the 937 nm channel is used to derive the water vapor optical depth (WVOD, $\tau_{PWV}$). In the derivation of WVOD, Equation (3) is expressed as Equation (8), because other gaseous absorptions are negligible and water vapor absorption is strong at this wavelength:

$$\tau_{TOD} = \tau_{Rayleigh} + \tau_{aerosol} + \tau_{PWV} \tag{8}$$

WVOD can be expressed as Equation (9), denoting the column water vapor and including the optical pass length by water vapor ($m_w$), and constants a and b [32]:

$$\tau_{PWV} \approx a \times (m_w u)^b \tag{9}$$

In the case of the Zuunmod field campaign, a discontinuous pattern was found after 3:00 UTC, because unrealistic TOD values were recorded. According to the MFRSR measurements of Zuunmod,

stable clear skies were detected, indicating that we can select the value for water vapor at the time closest to the KOMPSAT-3A passing time, by assuming that the variation in column water vapor is insignificant. Table 3 shows selected values for AOD, water vapor, and ozone at satellite overpass times, for the Goheung and Zuunmod sites.

**Table 3.** Atmospheric conditions of KOMPSAT-3A for input parameters of 6S simulation.

| Date | Aerosol Optical Depth (550 nm) | Water Vapor (g/cm$^2$) | Ozone (cm-atm) |
|---|---|---|---|
| 27 May 2015 | 0.12 | 0.38 | 287.03 |
| 18 June 2015 | 0.07 | 0.99 | 301.07 |

### 2.5. Retrieval of PSF with KOMPSAT-3A MS Bands by Observing Stars

The PSF, which is the electronic response of a sensor system to a point radiator, is an important criterion of image quality [40]. How well the PSF is defined is also important, as the PSF of the CCD camera can seriously affect the accuracy of radiometric calibration and measurement [41]. In addition, the impact of the PSF on the optical sensor results in considerable uncertainties in derived MODIS land cover products [42]. Therefore, we also newly considered the effects of the PSF by observing images of a point source, such as a bright star, to characterize the AEISS-A sensor response to the point source [43,44]. We observed stars using KOMPSAT-3A MS to measure the PSF of the AEISS-A sensor during the IOT periods. The satellite attitude control system can be used to observe stars by rotating KOMPSAT-3A during Eclipse orbits. To select an effective bright star source, we first eliminated background noise, and then applied a threshold value by considering a high signal-to-noise ratio (SNR) and an unsaturated DN value. To select stars with radiances within the detection range of AEISS-A, we referred to the Gunn & Stryker Stellar spectrophotometric atlas, which contains information on the visible spectra of 175 stars [45]. Figure 9 shows measured star images from the KOMPSAT-3A-combined MS bands. Figure 9h shows the overlaid KOMPSAT-3A MS images of selected stars, and the highest points of the images are the locations of the stars. Based on Figure 9h, $3 \times 3$ pixels were the sensitive area for PSF effects, indicating that the adjacency effects can be reduced and PSF compensated for, by using tarps that are large enough, such as those occupying $5 \times 5$ pixels ($11 \times 11$ m in the nadir direction in the KOMPSAT-3A MS images) or more.
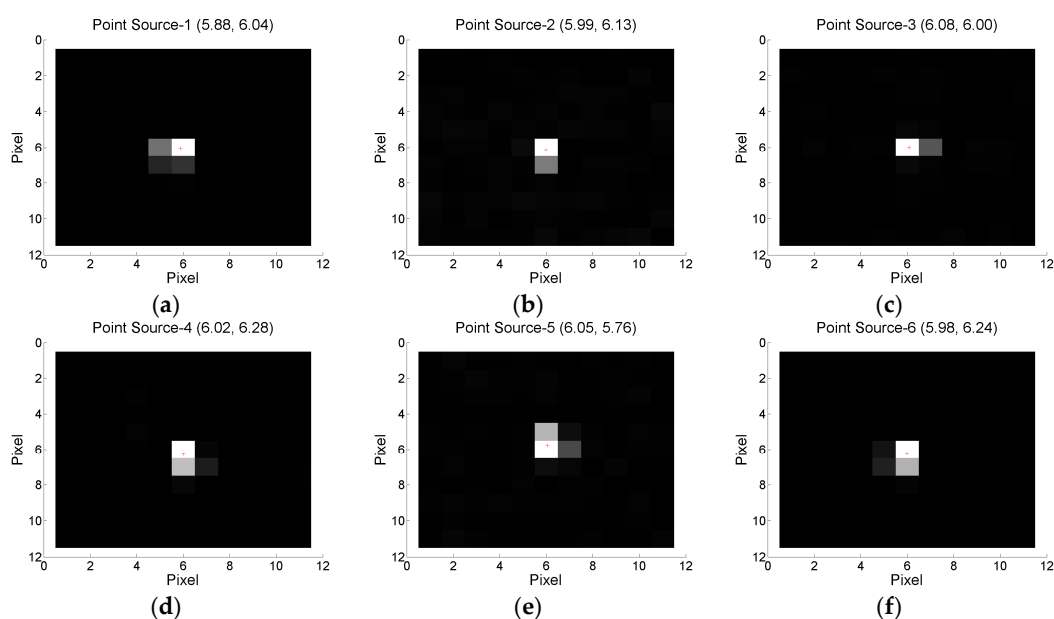


**Figure 9.** *Cont.*
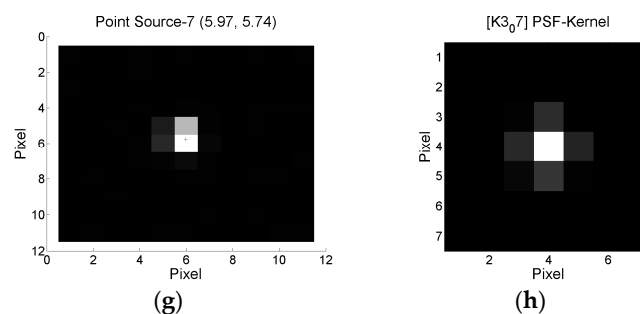
**Figure 9.** MS images over selected stars during IOT periods are shown from (**a**) to (**g**). The red cross in each image is the location of the star. (**h**) shows the overlaid KOMPSAT-3A MS images of selected stars.

To reduce the diffraction effects by AEISS-A CCD sensor characteristics, the PSF of the KOMPSAT-3A MS was generated from the star image data acquired by the MS bands of KOMPSAT-3A. Figure 10a shows the observed PSF of KOMPSAT-3A AEISS-A, as a function of radius at 25% full width and half maximum (FWHM). Although not a circle, the shape of the PSF is similar to a circularly symmetric Gaussian-like shape. Then, converting the matrix of the PSF based on star observations, the optical transfer function (OTF) of the system was simulated by Fourier transformation of the simulated PSF in Figure 10b. The MTF of KOMPSAT-3A MS was determined by the magnitude of calculated OTF.
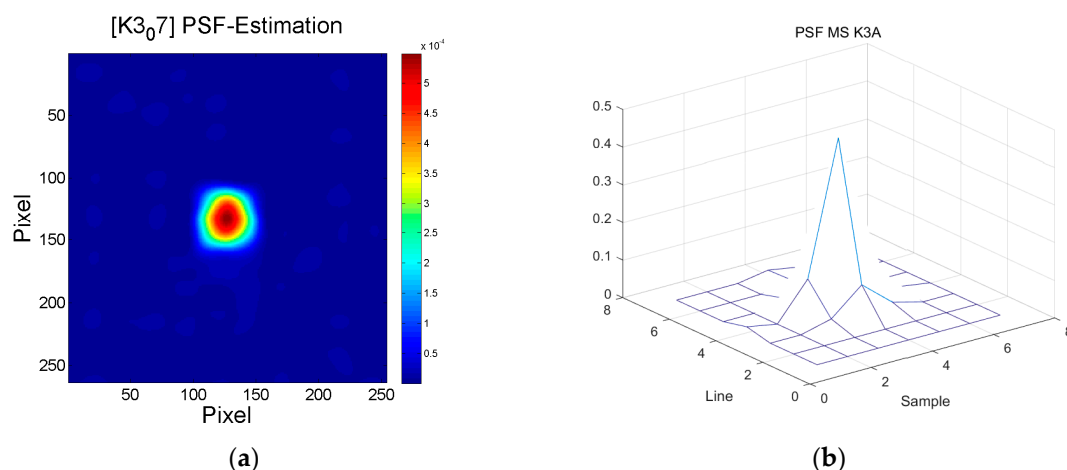


**Figure 10.** The shape of the PSF at 25% FWHM using star measurements (**a**) and the simulated PSF of KOMPSAT-3A MS bands with the Wiener filter (**b**).

Finally, by dividing the Fourier-transformed KOMPSAT-3A MS image in the frequency domain by the determined MTF, we calculated the satellite image data compensating for the PSF effect. The focusing system of the AEISS-A mainly depended on the temperature of the sensor focal lens, as we did not consider that the PSF change caused the temperature of the sensor focal lens, because its variation is nonlinear.

## 3. Results

Based on the vicarious radiometric calibration of KOMPSAT-3A, we simulated TOA radiance using the 6S model with the aforementioned input parameters, and estimated a match-up dataset using KOMPSAT-3A DN during the first Goheung field campaign. Figure 11 shows scatterplots of KOMPSAT-3A DNs and simulated radiance at the sensor over each of the deployed radiometric tarps, for all MS bands during the first Goheung field campaign. To estimate the DN-to-radiance

coefficients of this campaign, we performed a linear least squares fit using those estimated values. All scatterplots of the spectral bands are closely located over the linear regression lines, indicating that the four distinct radiometric tarps are useful for determining DN-to-radiance coefficients. In addition, all of the coefficients of determination have $R^2$ values close to 1.0. To test our values statistically, we performed the DN-to-radiance conversion twice: once using ANIF correction, and once without it. We expected that the effectiveness of the laboratory-based BRDF values applied would be checked by comparing the DN-to-radiance coefficients (ANIF correction or not) with the results of the second field campaign. The determied DN-to-radiance coefficients for the first Goheung field campaign are shown in Table 4. In this study, only gain values were calculated, because the calculated offset values are remarkably small and would be ignored when the values are finally converted to radiance.
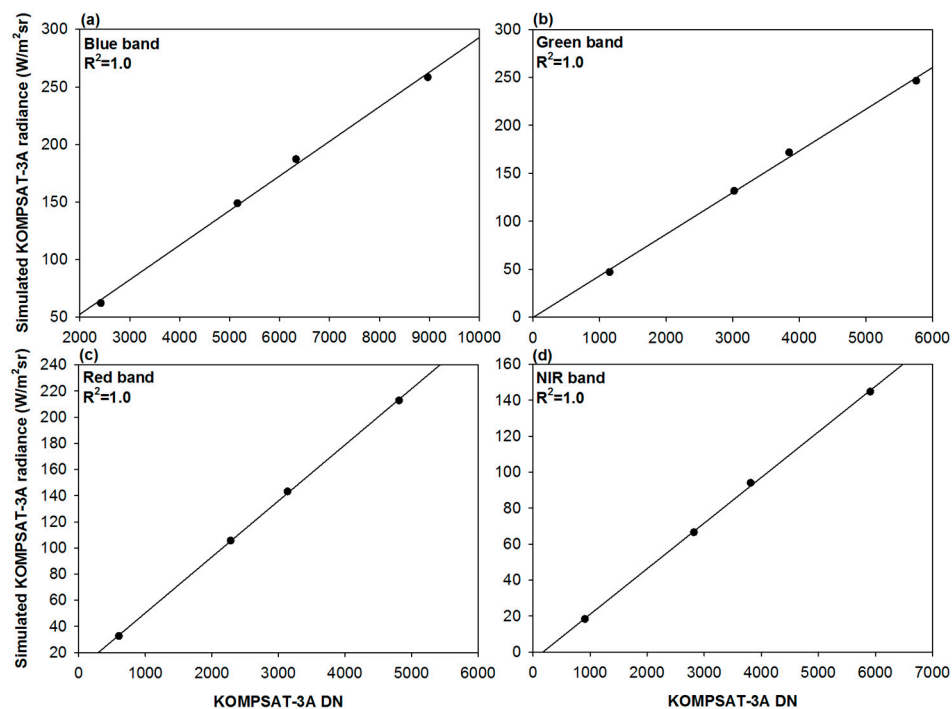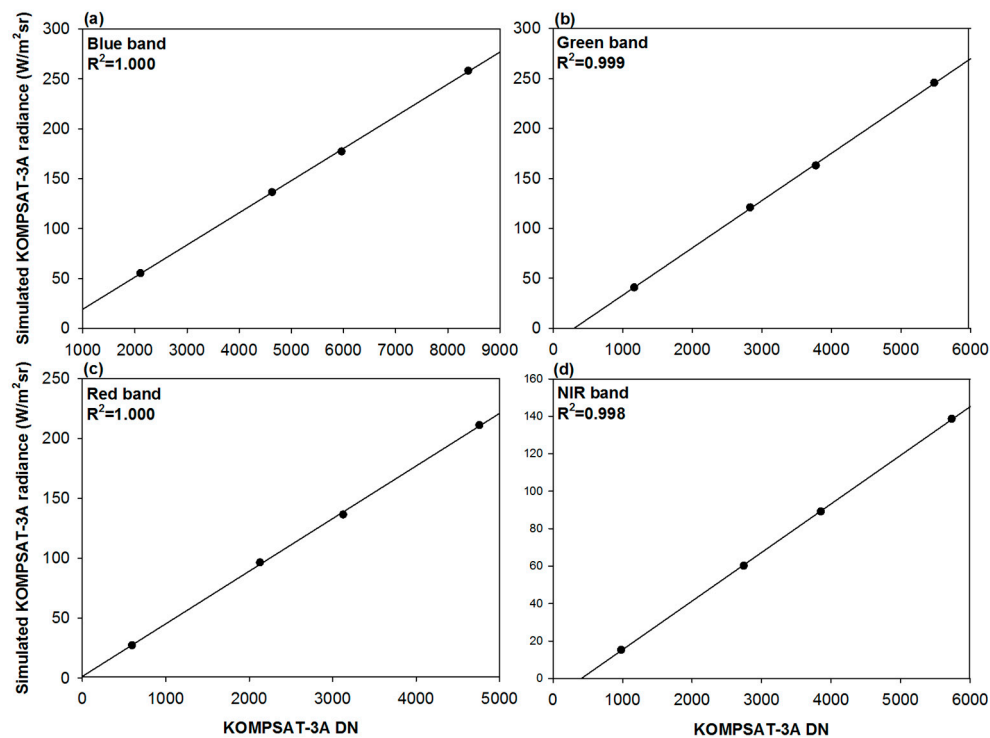


**Figure 11.** Scatterplots of KOMPSAT-3A DNs and simulated radiance at the sensor for all spectral bands during the first Goheung field campaign. (**a–d**) show blue, green, red, and NIR bands, respectively.

**Table 4.** Estimated radiometric calibration coefficients (scale) and coefficients of determination from KOMPSAT-3A DNs during the first field campaign.

| Spectral Band | Scale Factor (ANIF-Corrected) | $R^2$ (ANIF-Corrected) |
|---|---|---|
| Blue | 0.0285 (0.0289) | 0.999 (1.000) |
| Green | 0.0429 (0.0434) | 1.000 (1.000) |
| Red | 0.0446 (0.0450) | 1.000 (1.000) |
| NIR | 0.0242 (0.0244) | 1.000 (1.000) |

For the second field campaign over Zuunmod, Mongolia, we also estimated DN-to-radiance coefficients based on the same vicarious calibration methods and data formulation. As shown in Figure 12, the scatterplots between DN and simulated TOA radiance for each radiometric tarp also fitted the regression line, similar to the results of the Goheung field campaign. The $R^2$ values of the blue, green, red, and NIR bands, were 0.999, 1.0, 0.999, and 0.998, respectively, similar to the Goheung results. The various reflectance ranges of each tarp, from 4% to 60%, were effective for simulating the linear patterns of match-up data between DN and simulated radiance. As mentioned preiovusly, the estimated coefficients can be used in most cases of natural reflectance, as the reflectance of land is

usually less than 60%. However, it is difficult to model nonlinear characteristics, such as saturation, using the proposed coefficients for observing natural reflectors of 60% or more.



**Figure 12.** Scatterplots of KOMPSAT-3A DNs and simulated radiance at the sensor for all spectral bands during the second Zuunmod field campaign: (**a–d**) show the blue, green, red, and NIR bands, respectively.

We also calculated the gain ratio between the first and second campaign, to check the radiometric calibration continuity between the two field campaigns and to determine the effectiveness of the laboratory-based BRDF applied to the satellite observations. As we expected, the gain ratio of the ANIF-corrected scale factors was more reliable than the non-corrected values, particularly for the blue and green bands. The contributions of the laboratory-based BRDF corrections to the red and NIR bands were nonsignificant, which would be expected because of the ANIF values close to 1 based on Figure 5e,g. Consequently, the gain ratio between the two field campaigns in the last column of Table 5, had less than a 5% discrepancy for ANIF-corrected values, indicating that the DN-to-radiance conversion coefficients for KOMPSAT-3A are reasonable for estimating continuous variables for quantitative applications, such as surface reflectance, vegetation index, and atmospheric information.

**Table 5.** Estimated radiometric calibration coefficients (scale), coefficients of determination from KOMPSAT-3A DNs during the second field campaign, and gain ratios between the first and second campaigns (calculated as the first over the second values).

| Spectral Band | Scale Factor | $R^2$ | Gain Ratio between First and Second Field Campaign (ANIF-Corrected) |
|---|---|---|---|
| Blue | 0.0301 | 1.000 | 0.947 (0.960) |
| Green | 0.0438 | 0.999 | 0.979 (0.991) |
| Red | 0.0443 | 1.000 | 1.006 (1.015) |
| NIR | 0.0235 | 0.998 | 1.030 (1.038) |

## 4. Discussion

### 4.1. Approximate Error Budget of Vicarious Calibration for KOMPSAT-3A

We estimated the approximate error budget of the vicarious radiometric calibration with KOMPSAT-3A, in order to acknowledge the uncertain accuracy of the DN-to-radiance coefficient results. We considered worse-case conditions to inform users that these errors exist. Table 6 lists the evaluated approximate error sources of the vicarious calibration with KOMPSAT-3A MS bands. Basically, before performing vicarious calibration of KOMPSAT-3A, KARI implemented relative radiometric corrections to improve the categorical variables of imagery, mainly for non-uniformity, and the pixel burst, which change the quality of the DN values after processing. Non-uniformity correction (NUC) was performed to reduce non-uniformity and eliminate sparkle lines, because the assembled CCD sensor of the AEISS-A generally shows variation between detectors, which appear in the along-track direction of scanning [17]. Furthermore, for pixel burst, an image data restoration (de-noising) algorithm was applied to minimize the pattern noise, by selecting dark DN areas. We assigned a 5% error value to that induced by performing relative radiometric correction, which was analyzed during the IOT periods. We did not interpret the effects of relative radiometric accuracy assessment, but rather focused on the absolute radiometric calibration results of KOMPSAT-3A. Second, as recommended by the CEOS community, we utilized the solar irradiance profile derived from Thuillier et al. [2], to convert the at-sensor spectral radiance to TOA reflectance. We assigned a 3% radiance error, considering the inherent solar irradiance data uncertainty and the spectral wavelength resolution discrepancy between 1 nm solar irradiance data of Thuillier et al. [2], and the 6S radiative transfer model of 2.5 nm resolution. In the case of the exo-atmospheric solar spectral irradiances for KOMPSAT-3A, we used the same values of KOMPSAT-3, due to the same SRF of the sensor.

When using the hyperspectral reflectance of the radiometric tarps by the ASD FieldSpec® 3 for the radiative transfer model, peak-to-peak reflectance variation exists within the SRF wavelength ranges of the MS bands. The variation in hyperspectral reflectance for each corresponding band, was less than 1% for all radiometric tarps. The spatial variability of the hyperspectral reflectance of the radiometric tarps was also measured using ASD FieldSpec® 3. The reflectance between any two points on the tarps varied by less than 1%. Therefore, we assigned a value of 1% to the surface reflectance measurement and used it in the simulation model. The measurements of hyperspectral reflectance on the radiometric tarps with the ASD FieldSpec® 3 could generate radiometric uncertainty that directly propagates to the calibration results for the following reasons. The single use of the ASD FieldSpec® 3 can introduce error, due to the measurement time difference between the downward and upward hyper-radiance. To measure the hyperspectral reflectance, the ASD FieldSpec® 3 observes the Spectralon white panel for downward radiance measurement, and then observes the upward radiance on tarps. However, during the measurement interval, if weather conditions change, mainly due to rapidly moving clouds, the measurement reflectance accuracy of a single ASD FieldSpec® 3 could be reduced. For the purpose of future work, we would prepare two ASD FieldSpec® 3 spectroradiometers, in order to reduce the limitations of a single unit. In this study, we merely mention the potential error of field measurements; we did not include the uncertain accuracy in the error budget because the measurement accuracy of the ASD FieldSpec® 3 is observer-dependent, and it is difficult to quantify the amount of error. Instead, we only determined that the inherent device accuracy of the ASD FieldSpec® 3 is less than 1%.

We also used laboratory-based BRDF measurements of the radiometric tarps to normalize the satellite-based reflectances to the nadir geometry of the ASD FieldSpec® 3 for the Goheung field campaign. Although the lab measurements were useful for compensating for discrepancies in observation geometry, the uncertainties of the radiometric tarps still remained. We assigned a value of 2.5%, which is the maximum value of uncertainty based on laboratory-based BRDF measurements. Furthermore, based on the results shown in Figures 4 and 5, it is notable that the laboratory-based BRDF measurements of the tarps showed symmetry patterns that were the inverse of the detection angle as the center of the nadir detection angle, indicating that the effects of the radiometric tarps on

BRDF would exist for the azimuth angle direction. For the effects in the azimuth direction, which are difficult to measure using a 2D hyperspectral gonioradiometer, undefined error factors remain, despite analyzing the uncertain accuracy of the laboratory-based BRDF. According to Georgiev and Butler [27], the greater the viewing zenith angle, the greater the BRDF effects in the azimuth angle direction. Therefore, we remind the user group about the inherent uncertainty associated with the azimuth direction, due to limitations of the 2D hyperspectral gonioradiometer.

Finally, we also represented the expected uncertainties of atmospheric measurements of AOD, ozone, and water vapor. For the AOD measured by MFRSR, we considered the radiometric error values, in spite of the applied Langley$_{MVC}$, to estimate the TOA irradiance, because uncertainties about the correction algorithm and inherent instrument would be expected. We assigned a 1% accuracy of AOD estimation with MFRSR. An error of WVOD at 937 nm would also be expected, due to the assumption that the effects of other gaseous absorptions are negligible and that water vapor absorption is strong over the 937 nm wavelength range. Furthermore, due to the missing value of column water for the Zuunmod site, we chose the nearest value to the satellite pass time, by assuming that the variation in column water vapor is insignificant in stable weather conditions. We also assigned a 10% accuracy of water vapor retrieval using MFRSR, according to Alexandrov et al. [46]. In the case of total ozone, we used the TOMS/OMI total ozone products for absorption of ozone, which have a 2% root mean square error (RMSE) with a horizontal resolution of $1°–1.2°$ (TOMS Ozone Algorithm Theoretical Basis Document, [47]). The corresponding TOA radiance errors with the controlled error values of AOD, column water vapor, and total ozone, are 1%–2%. The error for each atmospheric component was analyzed separately, using the 6S radiative transfer model. The sensitivity test method was applied to fix the other variables and to apply the extreme value of the corresponding variables.

**Table 6.** Approximate error budget for the vicarious calibration of KOMPSAT-3A.

|  | Accuracy (%) | Radiance Error (%) |
|---|---|---|
| Relative radiometric correction | 5 | 5 |
| Solar irradiance data | 3 | 3 |
| Surface reflectance measurement | 1 | 1 |
| Laboratory-based BRDF measurements | 2.5 | 2.5 |
| ASD FieldSpec® 3 instrument | 1 | 1 |
| 6S Radiative transfer | 1 | 1 |
| Aerosol optical depth from MFRSR | 1 | <1 |
| Total ozone from OMI ozone | 2 | <1 |
| Column water vapor amounts from MFRSR | 10 | <1 |
| Combined error |  | ~6.8 |

In the final analysis, the combined error of the vicarious calibration with KOMPSAT-3A MS was approximately 6.8%, assuming that each of the aforementioned error sources was independent. Therefore, it was calculated using the root of the squared sum of each error variable.

## 4.2. Limitation of Vicarious Calibration of KOMPSAT-3A

We did not perform cross-calibration, which is another proven calibration method, using the radiometrically calibrated Landsat-8 Operational Land Imager (OLI) [48] to calibrate KOMPSAT-3A. Various studies have performed cross-calibration with well-calibrated satellites [49–53]. Recently, Landsat-8 OLI was considered a reliable calibrated reference and showed reliable calibration results [54]. We considered cross-calibration using radiometrically calibrated Landsat-8 OLI to improve the radiometric calibration of KOMPSAT-3A. Among the various natural targets, we considered a desert area for cross-calibration because it meets the stability and homogeneity criteria, and the low cloudiness and characterized BRDF behavior would also be useful [55,56]. From among 20 desert sites selected by Cosnefroy et al. [57], we selected the Libya site, and used reported cross-calibration methods [17,52,58]. No cases met the requirements of the geometrical criteria [52], indicating that the increased BRDF

effects of surface and atmospheric loading would make it difficult to accurately simulate the TOA radiance, due to increased uncertainties of those error factors. As mentioned previously, the main reason for the geometrical discrepancy is the difference in equatorial crossing time between the KOMPSAT-3A ascending node at 1:30 p.m. local time, and the Landsat-8 descending node at 10:00 a.m. local time, which made it difficult to perform cross-validation in this study. Therefore, we could not perform the proven cross-calibration with Landsat-8 OLI, in order to improve the radiometric calibration of KOMPSAT-3A MS.

### 5. Summary and Conclusions

The radiometric characteristics of the KOMPSAT-3A MS bands were interpreted, based on vicarious calibration methods using the 6S radiative transfer model, well-known radiometric tarps, and MFRSR measurements. During the IOT periods, we determined KOMPSAT-3A DN-to-radiance coefficients, which will be useful for quantitative applications of the user group, over the two field campaigns. Laboratory-based BRDF measurements of the radiometric tarp samples, obtained using a hyperspectral gonioradiometer, were used to normalize satellite geometry-dependent reflectance to nadir-only ASD FieldSpec® 3 observations for high viewing angles. In addition, the modeled PSF, obtained by observing bright stars, was utilized to clarify the PSF and correct MS bands, in order to reduce the interfering radiance from targets adjacent to the tarps. The precise atmospheric conditions using MFRSR were also used to estimate related optical loadings of each gas in the wavelength range of KOMPSAT-3A SRF. The final statistical values for scale factors and $R^2$ were determined, based on the two field campaigns. The $R^2$ values of blue, green, red, and NIR bands for all cases, were more than 0.998, meaning that the suggested method is useful for determining the radiometric calibration of KOMPSAT-3. Particularly, we paid attention to the effectiveness of laboratory-based BRDF correction for higher viewing zenith angles. The gain ratios of the blue and green bands were improved to 1.3% and 1.2%, respectively, by applying ANIF correction. Finally, the calculated gain ratios between the first and second campaigns showed a discrepancy of less than 5%, indicating that the radiometric characteristics of KOMPSAT-3A are reasonable for estimating continuous variables for quantitative applications. Although we performed radiometric calibration carefully, uncertainty error remained in our methods, modeling, input parameters, and measurements. Thus, we also analyzed the approximate error budget for the vicarious calibration of KOMPSAT-3A, and assigned a value of 6.8%. These results should be useful to the user group when utilizing KOMPSAT-3A MS imagery.

**Author Contributions:** Jong-Min Yeom developed the research plan and supervised the work. Jong-Min Yeom analyzed data and prepared the manuscript and figures. Jisoo Hwang, Jae-Heon Jung, Kwon-Ho Lee, and Chang-Suk Lee participated in the literature review, data acquisition, method selection, and discussions. All authors were equally involved in the editing of the manuscript.

**Conflicts of Interest:** The authors declare no conflict of interest.

### References

1. Rees, W.G. *Physical Principles of Remote Sensing*, 2nd ed.; Cambridge University Press: Cambridge, UK, 2001.
2. Thuillier, G.; Hersé, M.; Labs, D.; Foujols, T.; Peetermans, W.; Gillotay, D.; Simon, P.C.; Mandel, H. The solar spectral irradiance from 200 to 2400 nm as measured by the SOLSPEC spectrometer from Atlas and Eureca missions. *Sol. Phys.* **2003**, *214*, 1–22. [CrossRef]
3. Liu, C.C.; Kamei, A.; Hsu, K.H.; Tsuchida, S.; Huang, H.M.; Kato, S.; Nakamura, R.; Wu, A.M. Vicarious calibration of the Formasat-2 remote sensing instrument. *IEEE Trans. Geosci. Remote Sens.* **2010**, *48*, 2162–2169.
4. Rao, C.R.N.; Chen, J.; Sullivan, J.T.; Zhang, N. Post-launch calibration of meteorological satellite sensors. *Adv. Space Res.* **1999**, *23*, 1357–1365. [CrossRef]
5. Markham, B.L.; Helder, D.L. Forty-year calibrated record of earth-reflected radiance from Landsat: A review. *Remote Sens. Environ.* **2012**, *122*, 30–40. [CrossRef]

6.   Dinguirard, M.; Slater, P.N. Calibration of space-multispectral imaging sensors: A review. *Remote Sens. Environ.* **1999**, *68*, 194–205. [CrossRef]

7.   Bowen, H.S. Absolute radiometric calibration of the IKONOS sensor using radiometrically characterized stellar sources. In Proceedings of the Pecora 15/Land Satellite Information IV/ISPRS Commission I/FIEOS 2002 Conference, Denver, CO, USA, 10–15 November 2002.

8.   Pagnutti, M.; Ryan, R.E.; Kelly, M.; Holekamp, K.; Zanoni, V.; Thome, K.; Schiller, S. Radiometric characterization of IKONOS multispectral imagery. *Remote Sens. Environ.* **2003**, *88*, 53–68. [CrossRef]

9.   Teillet, P.M.; Fedosejevs, G.; Thome, K.J.; Barker, J.L. Impacts of spectral band difference effects on radiometric cross-calibration between satellite sensors in the solar-reflective spectral domain. *Remote Sens. Environ.* **2007**, *110*, 393–409. [CrossRef]

10.  Mattar, C.; Hernández, J.; Artigas, A.S.; Alarcón, C.D.; Guerra, L.O.; Inzunza, M.; Tapia, D.; Lavín, E.E. A first in-flight absolute calibration of the Chilean Earth Observation satellite. *ISPRS J. Photogramm. Remote Sens.* **2014**, *92*, 16–25. [CrossRef]

11.  Kerola, D.X.; Bruegge, C.J.; Gross, H.N.; Helmlinger, M.C. On-orbit calibration of the EO-1 Hyperion and Advanced Land Imager (ALI) sensors using the LED Spectrometer (LSpec) automated facility. *IEEE Trans. Geosci. Remote Sens.* **2009**, *47*, 1244–1255. [CrossRef]

12.  Seo, S.B. Relative compensation method for degradation of visible detectors using improved direct histogram specification. *Electron. Lett.* **2014**, *50*, 446–447. [CrossRef]

13.  Ham, S.H.; Sohn, B.J. Assessment of the calibration performance of satellite visible channels using cloud targets: Application to Meteosat-8/9 and MTSAT-1R. *Atmos. Chem. Phys.* **2010**, *10*, 11131–11149. [CrossRef]

14.  Chavez, P.S. Image-based atmospheric corrections revisited and improved. *Photogramm. Eng. Remote Sens.* **1996**, *62*, 1025–1036.

15.  Kim, J.G.; Sohn, B.J.; Chung, E.S.; Chun, H.W. Simulation of TOA visible radiance for the ocean target and its possible use for satellite sensor calibration. *Korean J. Remote Sens.* **2008**, *24*, 535–549.

16.  Vermote, E.F.; Tanré, D.; Deuzé, J.L.; Herman, M.; Morcette, J.J. Second simulation of the satellite signal in the solar spectrum, 6S: An overview. *IEEE Trans. Geosci. Remote Sens.* **1997**, *35*, 675–686. [CrossRef]

17.  Yeom, J.M.; Hwang, J.; Jin, C.G.; Han, K.S. Radiometric characteristics of KOMPSAT-3 multispectral images using the spectra of well-known surface tarps. *IEEE Trans. Geosci. Remote Sens.* **2016**, *54*, 5914–5924. [CrossRef]

18.  Nandy, P.; Thome, K.; Biggar, S. Characterization and field use of a CCD camera system for retrieval of bidirectional reflectance distribution function. *J. Geophys. Res.* **2001**, *106*, 11957–11966. [CrossRef]

19.  Pagnutti, M.; Holekamp, K.; Blonski, S.; Sellers, R.; Davis, B.; Zanoni, V. Measurement sets and sites commonly used for characterizations. *ISPRS Arch.* **2002**, *XXXIV*, 6.

20.  Feng, M.; Sexton, J.O.; Huang, C.; Masek, J.G.; Vermote, E.F.; Gao, F.; Narasimhan, R.; Channan, S.; Wolfe, R.E.; Townshend, J.R. Global surface reflectance products from Landsat: Assessment using coincident MODIS observations. *Remote Sens. Environ.* **2013**, *134*, 276–293. [CrossRef]

21.  Kotchenova, S.Y.; Vermote, E.F.; Matarrese, R.; Klemm, F.J. Validation of a vector version of the 6S radiative transfer code for atmospheric correction of satellite data. Part I: Path radiance. *Appl. Opt.* **2006**, *45*, 6762–6774. [CrossRef] [PubMed]

22.  Seidel, F.C.; Kokhanovsky, A.A.; Schaepman, M.E. Fast and simple model for atmospheric radiative transfer. *Atmos. Meas. Tech.* **2010**, *3*, 1129–1141. [CrossRef]

23.  Vermote, E.F.; Kotchenova, S. Atmospheric correction for the monitoring of land surfaces. *J. Geophys. Res.* **2008**, *113*, D23S90. [CrossRef]

24.  Second Simulation of a Satellite Signal in the Solar Spectrum-Vector (6SV). Available online: http://6s.ltdri.org/files/tutorial/6S_Manual_Part_1.pdf (accessed on 3 February 2017).

25.  Clark, B.; Suomalainen, J.; Pellikka, P. The selection of appropriate spectrally bright pseudo-invariant ground targets for use in empirical line calibration of SPOT satellite imagery. *ISPRS J. Photogramm. Remote. Sens.* **2011**, *66*, 429–445. [CrossRef]

26.  Wu, A.; Li, Z.; Cihlar, J. Effects of land cover type and greenness on advanced very high resolution radiometer bidirectional reflectances: Analysis and removal. *J. Geophys. Res.* **1995**, *100*, 9179–9192. [CrossRef]

27.  Georgiev, G.T.; Butler, J.J. Laboratory-based bidirectional reflectance distribution functions of radiometric tarps. *Appl. Opt.* **2008**, *47*, 3313–3323. [CrossRef] [PubMed]

28. Feingersh, T.; Dorigo, W.; Richter, R.; Dor, E.B. A new model-driven correction factor for BRDF effects in HRS data. In Proceedings of the EARSel Workshop, Warsaw, Poland, 27–30 April 2005.

29. Hwang, J.S. Absolute measurement of hyperspectral and angular reflection. *Appl. Opt.* **2014**, *53*, 6216–6221. [CrossRef] [PubMed]

30. Feingersh, T.; Schläpfer, D.; Bor, E.B. Towards operational BRDF correction for imaging spectrometry data. In Proceedings of the 6th EARSeL SIG IS Workshop, Tel Aviv, Israel, 16–18 March 2009.

31. Harrison, L.; Michalsky, J.; Berndt, J. Automated multifilter rotating shadow-band radiometer: An instrument for optical depth and radiation measurements. *Appl. Opt.* **1994**, *33*, 5118–5125. [CrossRef] [PubMed]

32. Alexandrov, M.D.; Schmid, B.; Turner, D.D.; Cairns, B.; Oinas, V.; Lacis, A.A.; Gutman, S.I.; Westwater, E.R.; Smirnov, A.; Eilers, J. Columnar water vapor retrievals from multifilter rotating shadowband radiometer data. *J. Geophys. Res.* **2009**, *114*, D02306. [CrossRef]

33. Koontz, A.; Flynn, C.; Hodges, G.; Michalsky, J.; Barnard, J. *Aerosol Optical Depth Value-Added Product*; United States Department of Energy: Washington, DC, USA, 2013.

34. Lee, K.H.; Li, Z.; Cribb, M.C.; Liu, J.; Wang, L.; Zheng, Y.; Xia, X.; Chen, H.; Li, B. Aerosol optical depth measurements in eastern China and a new calibration method. *J. Geophys. Res.* **2009**, *115*. [CrossRef]

35. Forgan, B.W. *Sun Photometer Calibration by the Ratio Langley Method, in Baseline Atmospheric Program*; Forgan, B.W., Fraser, P.J., Eds.; Bureau of Meteorology: Melbourne, Australia, 1988; pp. 22–26.

36. Hansen, J.E.; Travis, L.D. Light scattering in planetary atmospheres. *Space Sci. Rev.* **1974**, *16*, 527–610. [CrossRef]

37. Alexandrov, M.D.; Lacis, A.A.; Carlson, B.E.; Cairns, B. Remote sensing of atmospheric aerosols and trace gases by means of multifilter rotating shadowband radiometer. Part I: Retrieval algorithms. *J. Atmos. Sci.* **2002**, *59*, 524–543. [CrossRef]

38. Nicolet, M. The solar spectral irradiance and its action in the atmospheric photo dissociation processes. Planet. *Space Sci.* **1981**, *29*, 951–974. [CrossRef]

39. Vandaele, A.C.; Hermans, C.; Fally, S.; Carleer, M.; Colin, R.; Merienne, M.F.; Jenouvrier, A.; Coquart, B. High-resolution Fourier transform measurement of the $NO_2$ visible and near-infrared absorption cross sections: Temperature and pressure effects. *J. Geophys. Res.* **2002**, *107*, 43–48. [CrossRef]

40. Gaskill, J.D. *Linear Systems Fourier Transforms and Optics*; John Wiley: New York, NY, USA, 1978.

41. Du, H.; Voss, K.J. Effects of point-spread function on calibration and radiometric accuracy of CCD camera. *Appl. Opt.* **2004**, *43*, 665–670. [CrossRef] [PubMed]

42. Huang, C.; Townshend, J.R.G.; Liang, S.; Kalluri, S.N.V.; DeFries, R.S. Impact of sensor's point spread function on land cover characterization: Assessment and deconvolution. *Remote Sens. Environ.* **2002**, *80*, 203–212. [CrossRef]

43. Murchie, S.; Robinson, M.; Hawkins, S.E., III; Harch, A.; Helfenstein, P.; Thomas, P.; Peacock, K.; Owen, W.; Heyler, G.; Murphy, P.; et al. Inflight calibration of the NEAR multispectral imager. *Icarus* **1999**, *140*, 66–91. [CrossRef]

44. Li, H.; Robinson, M.S.; Murchie, S. Preliminary remediation of scattered light in NEAR MSI images. *Icarus* **2002**, *155*, 244–252. [CrossRef]

45. Gunn, J.E.; Stryker, L.L. Stellar spectrophotometric atlas, 3130 < 1 < 10800 A. *Astrophys. J. Suppl. Ser.* **1983**, *52*, 121–153.

46. Alexandrov, M.D.; Lacis, A.A.; Carlson, B.E.; Cairns, B. Characterization of atmospheric aerosols using MFRSR measurements. *J. Geophys. Res.* **2008**, *113*, D08204. [CrossRef]

47. TOMS Ozone Algorithm Theoretical Basis Document. Available online: http://projects.knmi.nl/omi/documents/data/OMI_ATBD_Volume_2_V2.pdf (accessed on 3 February 2017).

48. Pahlevan, N.; Lee, Z.; Wei, J.; Schaaf, C.B.; Schott, J.R.; Berk, A. On-orbit radiometric characterization of OLI (Landsat-8) for applications in aquatic remote sensing. *Remote Sens. Environ.* **2014**, *154*, 272–284. [CrossRef]

49. Thome, K.J.; Bigger, S.F.; Wisniewski, W. Cross comparison of EO-1 sensors and other earth resources sensors to Landsat-7 ETM+ using Railroad Valley Playa. *IEEE Trans. Geosci. Remote Sens.* **2003**, *41*, 1180–1188. [CrossRef]

50. Chander, G.; Xiong, X.; Angal, A.; Choi, J. Monitoring on-orbit calibration stability of the Terra MODIS and Landsat 7 ETM+ sensors using pseudo-invariant test sites. *Remote Sens. Environ.* **2010**, *114*, 935–939. [CrossRef]

51. Chander, G.; Mishra, N.; Helder, D.L.; Aaron, D.B.; Amit, A.; Choi, T.; Doelling, D.R. Applications of Spectral Band Adjustment Factors (SBAF) for cross-calibration. *IEEE Trans. Geosci. Remote Sens.* **2013**, *51*, 1267–1281. [CrossRef]

52. Lachérade, S.; Fougnie, B.; Henry, P.; Gamet, P. Cross calibration over desert sites: Description, methodology, and operational implementation. *IEEE Trans. Geosci. Remote Sens.* **2013**, *51*, 1098–1113. [CrossRef]

53. Mishra, N.; Helder, D.L.; Angal, A.; Choi, T.; Xiong, X. Absolute calibration of optical satellite sensors using Libya 4 pseudo invariant calibration site. *Remote Sens.* **2014**, *6*, 1327–1346. [CrossRef]

54. Mishra, N.; Haque, M.O.; Leigh, L.; Aaron, D.; Helder, D.; Markham, B. Radiometric cross calibration of Landsat 8 Operational Land Imager(OLI) and Landsat 7 Enhanced Thematic Mapper Plus (ETM+). *Remote Sens.* **2014**, *6*, 12619–12638. [CrossRef]

55. Henry, P.; Dinguirard, M.; Bidilis, M. SPOT multitemporal calibration over stable desert areas. In Proceedings of the SPIE International Symposium of Aerospace Remote Sensing, Orlando, FL, USA, 12–16 April 1993.

56. Cabot, F.; Hagolle, O.; Cosnefroy, H.; Briottet, X. Intercalibration using desertic sites as a reference target. In Proceedings of the Geoscience and Remote Sensing Symposium, Seattle, WA, USA, 6–10 July 1998.

57. Cosnefroy, H.; Leroy, M.; Briottet, X. Selection and characterization of Saharan and Arabian desert sites for the calibration of optical satellite sensors. *Remote Sens. Environ.* **1996**, *58*, 101–114. [CrossRef]

58. Henry, P.; Chander, G.; Fougnie, B.; Thomas, C.; Xiong, X. Assessment of spectral band impact in intercalibration over desert sites using simulation based on EO-1 Hyperion data. *IEEE Trans. Geosci. Remote Sens.* **2013**, *51*, 1297–1308. [CrossRef]